# Tracing the Cross-Talk Phenomenon of Vinylethylene Carbonate to Unveil its Counterintuitive Influence as an Electrolyte Additive on High-Voltage Lithium-Ion Batteries

Felix Pfeiffer, Angela Griggio, Matthias Weiling, Jian-Fen Wang, Friederike Reißig, Christoph Peschel, Lex Pillatsch, Stefan Warrington, Sascha Nowak, Valentine Grimaudo, Iain Wright, and Masoud Baghernejad\*

The formation of effective interphases is crucial to enable high-performance lithium-ion batteries. This can be facilitated by the introduction of electrolyte additives, ensuring improved stability and transport properties. The identification of proper additives requires a comprehensive understanding of the fundamental mechanisms of interfacial reactions governing interphase formation. This study presents a detailed investigation of widely known and less conventional interphase-forming additives in high-voltage LiNi<sub>0.6</sub>Mn<sub>0.2</sub>Co<sub>0.2</sub>O<sub>2</sub>, NMC622||artificial graphite cells. The electrochemical characterization shows that cells containing vinylethylene carbonate (VEC) significantly outperform all other investigated electrolyte formulations. Surprisingly, gas chromatography-mass spectroscopy measurements of the electrolyte composition after cycling indicate the formation of an ineffective solid-electrolyte interphase (SEI) in the presence of VEC. A thorough analysis of the interfacial composition via operando shell-isolated nanoparticle-enhanced Raman spectroscopy (SHINERS) and surface-enhanced Raman spectroscopy elucidates rather the formation of an effective cathode-electrolyte interphase (CEI). This phenomenon results from the reductive reaction of VEC on the anode, followed by the product transfer and electro-polymerization of reaction products on the cathode. Additionally, focused ion beam secondary ion mass spectrometry (FIB-SIMS) with a time of flight (ToF)-detector is used to analyze the elemental spatial distribution of Li-species and Mn in the respective SEIs.

# 1. Introduction

The electrode-electrolyte interphases formed on the surface of the negative and positive electrodes play a vital role in determining the cycle life and electrochemical performance of lithium-ion batteries (LIBs). These interphases passivate the electrode surfaces, reducing parasitic electrolyte degradation reactions and active lithium loss.[1-8] Conversely, the formation of unstable interphases can also lead to continuous electrolyte consumption, due to parasitic reactions and interphase (re-)formation during galvanostatic charge/discharge cycling, severely hampering the cycle life and performance of LIBs. The continuous interphase (re-)formation can also negatively impact LIB performance due to increased interfacial resistances and reduced Li-ion transport.[1,2,4,5] That being the case, the controlled formation of effective interphases is crucial for improving the cycle life and performance of LIBs. Introducing film-forming electrolyte additives is considered a promising

F. Pfeiffer, A. Griggio, M. Weiling, J.-F. Wang, F. Reißig, M. Baghernejad Helmholtz-Institute Münster

IEK-12

Forschungszentrum Jülich GmbH Corrensstraße 46, 48149 Münster, Germany

E-mail: b.masoud@fz-juelich.de

C. Peschel, S. Nowak

MEET Battery Research Center Münster

University of Münster

Corrensstraße 46, 48149 Münster, Germany



The ORCID identification number(s) for the author(s) of this article can be found under https://doi.org/10.1002/aenm.202402187

© 2024 The Author(s). Advanced Energy Materials published by Wiley-VCH GmbH. This is an open access article under the terms of the Creative Commons Attribution License, which permits use, distribution and reproduction in any medium, provided the original work is properly cited.

DOI: 10.1002/aenm.202402187

L. Pillatsch, V. Grimaudo TOFWERK AG Schorenstrasse 39, Thun CH-3645, Switzerland S. Warrington

Department of Chemistry
Loughborough University
Epinal Way, Loughborough, Leicestershire LE11 3TU, UK

I. Wright School of Chemistry University of Edinburgh

Joseph Black Building, David Brewster Road, Edinburgh EH9 3FJ, UK

ADVANCED ENERGY MATERIALS

www.advenergymat.de

approach toward controlled interphase formation.[5-11] Ethylene carbonate (EC)-based derivatives as fluoroethylene carbonate (FEC) and vinylene carbonate (VC) are already well known for their beneficial film-forming abilities and found widespread utilization, even in commercial applications, and have been investigated thoroughly.[5,10,12-17] Many of these studies shed light on the composition of the respective interphases, composed of specific decomposition products of the additives, e.g., LiF for FEC and polymeric species for FEC and VC.[10,11,16-20] While other EC derivatives like chloroethylene carbonate (ClEC) or vinylethylene carbonate (VEC) are also known in the literature, their interphase formation abilities have not been systematically evaluated. [21-24] Furthermore, it should be noted that the majority of the studies aiming to reveal the composition of additivebased interphases rely on postmortem and ex situ techniques for analysis. [10,18,20,21,23,25] Yet, a deep understanding of additivemediated interphase formation mechanisms and compositions under real working conditions is crucial for systematically investigating new electrolyte formulations and designing tailored additives. $[\bar{3},4,25]$ 

Operando vibrational spectroscopic techniques, such as Raman spectroscopy, hold great promise in providing chemical and structural information at the molecular level and unraveling the formation mechanisms of the interphase under real working conditions. However, hampered by the intrinsic limitations of the inefficient Raman scattering process, conventional Raman spectroscopy is inadequate in probing the chemical composition of interphases in LIBs. Due to very low intensities of the active Raman bands of interphase species, caused by a trace quantity of species at the nanometric thin interphase and low intrinsic Raman cross-section of such species, they are easily masked by the active Raman bands from the bulk electrode materials or the electrolyte components.[3,25-28] Advancements in near-field Raman spectroscopy techniques enable the characterization of materials at trace quantities by amplifying the signal in the vicinity of plasmonic active resonators such as gold and silver nanostructures. This phenomenon is known as surface-enhanced Raman spectroscopy (SERS) and has been employed in various studies to analyze interphases and electrolytes in LIBs.[3,25,29,30] However, it has to be noted that the dependence of SERS on metal substrates for signal enhancement restricts the application of this technique for the investigation of interphase on real electrode materials of LIBs. To overcome this constraint, SERS variants such as tipenhanced Raman spectroscopy, and shell-isolated nanoparticleenhanced Raman spectroscopy (SHINERS), have been developed and successfully employed in battery research, gaining valuable insights into interphases.<sup>[3,25,26,28,31,32]</sup> For example, one of the first studies utilizing SHINERS for solid-electrolyte interphase (SEI) analysis was presented by Cabo-Fernandez et al. identifying semi-carbonates, alkyl carboxylates, and PEOlike species as main components of the formed interphase.[33] Similar SEI products were also reported by Martin-Yerga et al., using an innovative combination of SHINERS and scanning electrochemical cell microscopy to characterize the evolving interphase.[34]

This study presents a detailed evaluation of how different EC-based derivatives impact the electrochemical performance of high-voltage  $\text{LiNi}_{0.6}\text{Mn}_{0.2}\text{Co}_{0.2}\text{O}_2$ , NMC622||artificial graphite (NMC622||AG) pouch cells containing carbonate-based elec-

trolytes. Our investigations demonstrate that incorporating an optimized concentration of VEC into the baseline electrolyte (BE, 1.0 M LiPF<sub>6</sub> in EC/EMC (3:7, by weight)) significantly improves the electrochemical performance and extends the cycle life of the LIB cells at high-voltage. Remarkably, the electrolyte formulations with VEC exhibit significantly enhanced cell performance compared to other electrolyte formulations with wellknown electrolyte additives, such as FEC and VC. Counterintuitively, gas-chromatography-mass spectrometry (GC-MS) investigations grasp oligomerization and transesterification products in the bulk electrolytes of BE and BE+VEC due to side reactions on the anode, indicating that VEC largely fails to form an effective SEI, unlike FEC and VC. Additionally, focused ion beam secondary ion mass spectrometry (FIB-SIMS) was performed to investigate the elemental spatial distribution of Li-species and transition metals in the respective additive-induced SEIs. The results indicate that in contrast to FEC and VC, VEC forms an ineffective SEI, as Li-species were detected in deeper layers of the interfacial region of the electrode. Instead, scanning electron microscopy (SEM) topography of the cathode surface shows the formation of an interphase on the cathode (cathode-electrolyte interphase, CEI) in the presence of VEC. The formation of this interphase is confirmed via operando SHINERS and SERS measurements, identifying semi-carbonates and alkyl-carbonates as main interphase components. Furthermore, our detailed analysis showed that the identified components of the VEC-induced CEI most likely originate from the initial decomposition of the additive on the anode side, followed by a cross-talk process of the decomposition products to the cathode. Importantly, the operando near-field Raman spectroscopy analysis indicated the electropolymerization of the VEC decomposition product on the cathode, possibly accounting for the observed enhancement in the cell performance in the presence of VEC.

### 2. Results and Discussion

### 2.1. Investigation of Electrochemical Performance

The effect of EC-based derivatives on the electrochemical performance of the high-voltage NMC622||artificial graphite pouch cells was investigated via galvanostatic charge/discharge cycling. Note that in Figure 1, only the electrolyte formulations with an optimized additive concentration are displayed. For a detailed presentation of the electrochemical performance of cells using different additive concentrations, please refer to Figure S2 (Supporting Information). A summary of the results of the electrochemical performance analysis can be found in Table 1 at the end of the section.

A comparison of the specific discharge capacities of the cells containing the optimized concentration of electrolyte additives is shown in Figure 1a. For the cells containing the BE, an initial (first cycle after formation cycles) specific discharge capacity of 159 mAh g $^{-1}$  was recorded, which continuously faded during ongoing cycling until reaching 80 mAh g $^{-1}$  (50% state-of-health, SoH) after 412 cycles. It is important to note that after  $\approx\!380$  cycles, an increase in the rate of capacity fading is observed. This escalating fading suggests failure mechanisms such as the formation of micro dendrites, caused by transition-metal dissolution into the electrolyte, or structural collapse of the cathode's

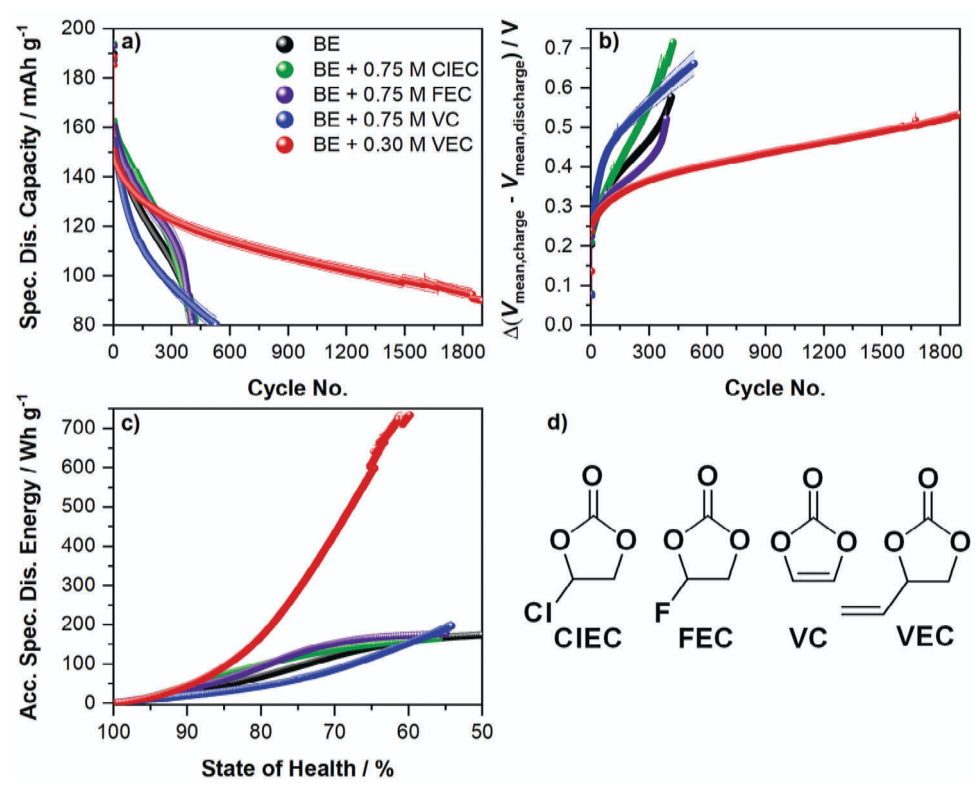


Figure 1. Results derived from the galvanostatic charge/discharge investigation of the various investigated electrolyte formulations with optimized additive concentration: BE (baseline electrolyte, 1 μ LiPF<sub>6</sub> in EC:EMC 3:7, black), BE + 0.75 μ CIEC (green), BE + 0.75 μ FEC (purple), BE + 0.75 μ VC (blue), and BE + 0.30 μ VEC (red). Depicted are: a) specific discharge capacities, b) the differential voltage analysis, and c) the accumulated specific discharge energy densities. d) Shows the molecular structures of the investigated carbonate-based additives.

active material, a phenomenon referred to as "roll-over" failure in the literature. These issues are frequently encountered in the cells with NMC cathode operated at high voltages. [35–37] For cells containing an optimized concentration of ClEC, a similar initial discharge capacity of 163 mAh g<sup>-1</sup> is observed. Compared to the BE cells, the ClEC cells exhibit a slower capacity fading during galvanostatic cycling. However, it is evident that rapid capacity fading occurs towards the end of the cells' lifespan, emerging as

**Table 1.** Summary of the results of the electrochemical performance analysis of the investigated electrolyte formulations: BE (baseline electrolyte, 1  $\,\rm M$  LiPF $_6$  in EC:EMC 3:7), BE + 0.75  $\,\rm M$  ClEC, BE + 0.75  $\,\rm M$  FEC, BE + 0.75  $\,\rm M$  VC, and BE + 0.30  $\,\rm M$  VEC. Denoted are the cycle life, average Coulombic efficiency (Ø CE, calculated without the CE of the formation cycles), mean charge/discharge voltage analysis (ΔV), and accumulated discharge energy density (ADE). All shown values are obtained from Figure 1 and represent 50% SoH, except for the VEC cells which show 60% SoH. All values were calculated based on the average of four cells. Standard deviations are not denoted in the following table, but always below 10%, and mostly below 5%.

Electrolyte	Cycle life	Ø CE/%	$\Delta V/\text{mV}$	ADE/Wh g <sup>-1</sup>
BE	412	99.9	578	174
+ 0.75 M CIEC	420 (+ <b>2</b> %)	99.6 ( <b>-0.3</b> %)	716 ( <b>+19</b> %)	166 ( <b>-5</b> %)
+ 0.75 м FEC	409 (-1%)	99.8 ( <b>-0.1</b> %)	523 (-11%)	177 ( <b>+2</b> %)
+ 0.75 м VC	531 ( <b>+29</b> %)	99.9 ( <b>-0.1</b> %)	663 ( <b>+13</b> %)	197 ( <b>+14</b> %)
+ 0.30 M VEC	1928 ( <b>+368</b> %)	99.9 (± <b>0</b> %)	537 ( <b>-8</b> %)	734 ( <b>+322</b> %)

early as 300 cycles, significantly sooner compared to the BE cells. Nevertheless, the CIEC cells reach their end-of-life (50% SoH) after ≈420 cycles, similar to the cells with BE. Interestingly, a comparable trend was observed for the FEC cells with an initial discharge capacity of 160 mAh g<sup>-1</sup>. Like their ClEC counterparts, the cells containing FEC exhibit a reduced discharge capacity fading during the ongoing charge/discharge cycling. However, the decrease in discharge capacity fading is marginally less pronounced compared to what is observed in the ClEC cells. Moreover, it is observed that the rapid capacity fading, indicating roll-over failure, occurs slightly later, ≈340 cycles, but exhibits a significantly steeper decline compared to the BE or ClEC cells. For the cells containing VC, a different trend is observed, as for CIEC and FEC. The VC cells exhibit lower initial capacities of 155 mAh g<sup>-1</sup>. In addition, these cells also show a faster rate of capacity fading compared to the BE cells, leading to lower discharge capacities for a majority of the cycling duration. Another distinction is evident in the VC cells, as no rapid capacity fading occurs towards the end of the cycle life. This absence of rapid fading is accompanied by a prolonged cycle life of ≈100 cycles. The electrochemical performance of the cells containing VEC in Figure 1a shows some similarities to the VC equivalents. For example, as observed for the VC cells, the initial discharge capacity of 150 mAh g<sup>-1</sup> is significantly lower compared to the BE cells. Moreover, no indication of roll-over failure is observed for the VEC cells until the endof-life. Nevertheless, the VEC cells exhibit a remarkably reduced capacity fading compared to the cells with BE and other EC-based

ADVANCED ENERGY MATERIALS

www.advenergymat.de

additives, outperforming all other considered systems by a significant margin. Whereas the other systems reach their respective end-of-life  $\approx\!400$  or 500 cycles, the VEC cells last for over 1900 cycles without even reaching 50% SoH (89 mAh g $^{-1}$ , 60% SoH at cycle 1900). It is worth noting that the optimized concentration for VEC is 0.30 M, which is considerably lower, compared to the other additives at optimized concentration.

Similar to the obtained discharge capacities, the Coulombic efficiencies (CEs) of the cells with different electrolyte formulations exhibit notable differences (Figure S3, Supporting Information). For the BE cells, a CE of 88% is obtained in the initial cycle. For the additive-based electrolyte formulations, slightly higher initial CEs of 89% are obtained for FEC and VC, while VEC (86%) and CIEC (83%) show lower initial CEs. Surprisingly, lower CEs are observed for the VEC cells in the 2nd and 3rd cycle, compared to the other electrolyte formulations showing similar CEs. This finding indicates additional parasitic reactions occurring in the VEC-containing cells. During ongoing charge/discharge cycling, similar CEs are obtained for all investigated cells (≈99.9%, Ø CE in Table 1), except the CIEC-containing cells showing a lower CE of 99.6%. Nevertheless, it has to be noted that the CE calculated for all additive-containing cells is (slightly) lower compared to the BE cells. This could be due to irreversible charge consumption due to the additives' decomposition. Moreover, toward the end of their cycling life, rapidly decreasing CEs are observed for the BE, ClEC, and FEC cells, being in good agreement with the rapid capacity decay observed in Figure 1a.

Evaluating the difference between the mean charge and discharge voltage ( $\Delta V$ ) is considered a robust way to gain insights into the internal resistance of the cells.[31,32,38,39] Internal resistance plays a crucial role in assessing electrolyte film-forming additives because resistive interphases can result in reduced electrochemical performances by causing higher over-voltages. The corresponding  $\Delta V$  values of the investigated electrolyte systems versus cycle number are depicted in Figure 1b, revealing significant differences. The cells containing BE, FEC, and ClEC exhibit comparable  $\Delta V$  values of 205, 225, and 210 mV for the initial cycle after formation. In contrast, the VC and VEC cells display notably higher  $\Delta V$  values of 250 and 240 mV, respectively. This could explain the observed loss of discharge capacity in the initial cycles, due to higher over-voltages. For higher cycle numbers, it is observed that the  $\Delta V$  values of the VEC cells are significantly lower compared to the other cells. Despite a significantly longer cycle life, the VEC-based cells exhibit a  $\Delta V$  of 537 mV at their end of life, while  $\Delta V$  values of 578, 715, 522, and 662 mV were recorded for the BE, ClEC, FEC, and VC cells respectively.

Summarizing the assessment of the various electrolyte additives poses a challenge due to the variety of parameters that can affect any specific cell's performance. Nonetheless, a straightforward way to compare the influence of different additives on the cell performance could be achieved by comparing accumulated specific discharge energies against the SoH, shown in Figure 1c. The accumulated discharge energy (ADE) value encompasses all associated effects of the electrolyte additives on the electrochemical performance of the cell system, allowing a straightforward evaluation. As already determined from the specific discharge capacity versus cycle number plot in Figure 1a, it is evident that the VEC cells significantly outperform the cells with other electrolyte systems, featuring prolonged cycle life and reduced dis-

charge capacity fading. The accumulated energy plot for cells with VEC outlines the enhanced performance, showing an accumulated discharge energy density surpassing 700 Wh g<sup>-1</sup> at 60% SoH. For the CIEC and FEC cells, a reduced capacity fading during the galvanostatic cycling results in initially higher capacity values and consequently higher discharge energy densities than BE cells. However, due to the increased capacity fading toward the end of their cycle life, the CIEC and FEC cells display comparable discharge energy densities of  $\approx 170$  Wh g<sup>-1</sup> at the end of their cycle life. For the VC cells, we observe the opposite effect. Due to initially increased capacity fading and therefore, lower discharge capacities, the VC cells exhibit reduced discharge energy densities throughout the initial galvanostatic cycles. Nevertheless, owning to the enhanced capacity retention toward the end, the VC cells indicate slightly higher energy density values of about 200 Wh  $g^{-1}$ , compared to the BE, ClEC, and FEC cells.

Further electrochemical characterization of the prepared electrolyte formulations was performed via cyclic voltammetry (CV) measurements (Figure S6, Supporting Information). CV measurements were performed in three-electrode cell systems with graphite as the working electrode (WE) and Li-metal as counter electrode (CE) and reference electrode (RE). The CV measurements exhibit an additional peak for all cells with the investigated electrolyte additives at 1.16, 1.03, 1.05, and 1.17 V versus Li|Li+for ClEC, FEC, VC, and VEC, respectively. These peaks occur at notably higher anode potentials compared to the EC-reduction peak (observed for the BE at 0.64 V vs. Li|Li+), and therefore indicate the reductive decomposition of all investigated additives before EC. A detailed analysis of the CV measurements can be found in the Supporting Information.

## 2.2. Electrolyte Investigation via GC-MS

To gain first insights into electrolyte and additive decomposition products, gas chromatography-mass spectroscopy (GC-MS) measurements were performed from aged electrolytes, as described in the Experimental Section. The recorded chromatograms are depicted in Figure 2.

For the aged BE, prominent peaks for the electrolyte solvents EC and EMC are detected. Moreover, the chromatogram exhibits distinct peaks assigned to dimethyl carbonate (DMC) and diethyl carbonate (DEC). The presence of these linear carbonates indicates ongoing transesterification reactions, resulting from the decomposition of EMC. In addition, peaks at higher retention times were detected, which are ascribed to different carbonate oligomers with increasing alkyl chain length, indicating the decomposition of EC. These peaks are also recorded in the GC chromatogram of the VEC electrolyte formulation, suggesting that ongoing electrolyte decomposition occurs also for this electrolyte system. For the electrolyte formulations containing ClEC, FEC, or VC, no peaks indicating the presence of DMC, DEC, or carbonate oligomers can be observed in the aged electrolyte. This suggests that the introduction of these additives to the electrolyte results in the formation of an SEI, which is effective in suppressing the reductive decomposition of the electrolyte solvents. The chromatograms also show that some additive molecules are still present in the electrolyte formulation after the 100th cycle, as a distinct peak is observed for each additive. In addition, for the

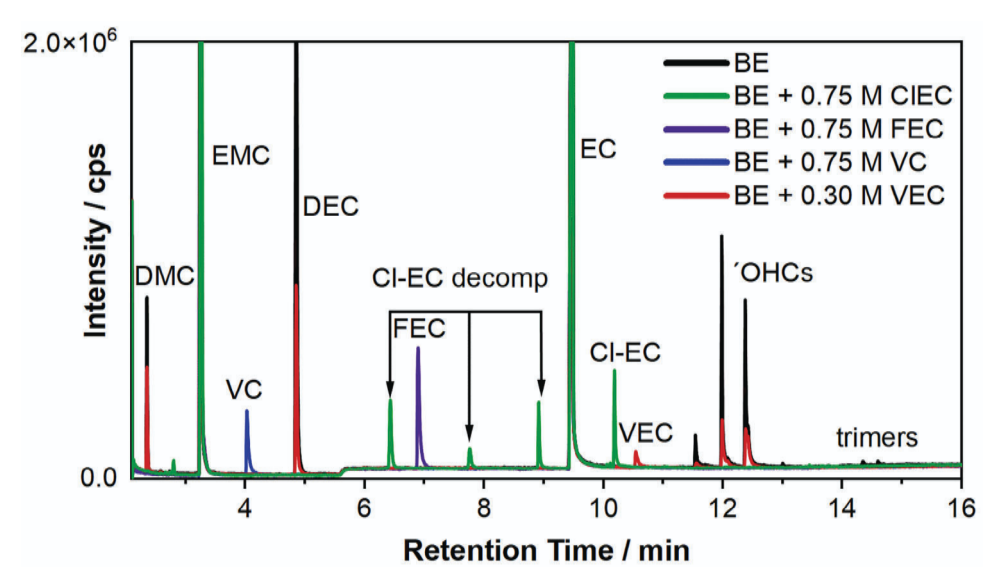


Figure 2. GC chromatograms of the electrochemically aged electrolyte formulations, extracted from NMC622||graphite pouch-cells after 100 charge/discharge cycles. BE (baseline electrolyte, 1 m LiPF<sub>6</sub> in EC:EMC 3:7, black), BE + 0.75 m CIEC (green), BE + 0.75 m FEC (purple), BE + 0.75 m VC (blue), and BE + 0.30 m VEC (red). Peak analysis was performed via mass spectrometry, dominant peaks are assigned in the depicted chromatogram Individual chromatograms of each electrolyte formulation are depicted in Figure S8 (Supporting Information).

CIEC sample characteristic decomposition products are identified. These were further analyzed with additional GC investigations with high-resolution-accurate mass detection and are discussed in detail in Figure S3 (Supporting Information).

The findings of the GC-MS investigations are rather surprising, especially if paired with the results of the galvanostatic cycling experiments. They indicate that VEC as the most effective additive to improve the cell's electrochemical performance, shows the least passivating SEI against reductive electrolyte decomposition. A possible explanation could be that rather than forming a passivating SEI, VEC instead forms an effective CEI, which accounts for the observed improvement in the electrochemical performance. To support this speculation, detailed investigations of the SEI and CEI were performed in the following sections.

### 2.3. Interphase Investigation

### 2.3.1. SEI Investigation

Initial investigations of the interphases formed on the surface of the graphite anodes in the presence of the different electrolyte formulations were performed via SEM. The obtained SEM images clearly show the formation of an SEI for all considered electrolyte formulations, exhibiting different morphologies. The SEM images, as well as a detailed description and analysis of the images, can be found in Figure S12 (Supporting Information).

Subsequently, operando SHINERS investigation of the surface of the anode during the first charge and in the presence of the different additive-containing electrolyte formulations was performed to analyze the composition of the formed interphases (**Figure 3**). The SHINER spectra exhibit a distinct influence of the presence of the respective additives on the SEI composition.

For the sake of clarity, we will only focus on active vibration bands which are characteristic and unique for the investigated electrolyte formulations (Figure 3a–e). The full range SHINER spectra and a detailed band assignment can be found in the SI in Figures S14–S18 and Tables S1–S5 (Supporting Information).

In the SHINER spectra of the anode's surface, charged in the presence of the BE (baseline electrolyte, 1  $\,\mathrm{m}$  LiPF<sub>6</sub> in EC:EMC 3:7, Figure 3a), a single characteristic band  $\approx 913~\mathrm{cm}^{-1}$  is observed, rising with increasing potential. According to the literature and our own reference spectrum, this band corresponds to O—C—O vibrations from diethyl 2,5-Dioxahexane dicarboxylate (DEDOHC), which is known as a typical decomposition product of EC.[28]

As shown in Figure 3b, the SHINER spectra of the SEI formed in the presence of CIEC exhibit several distinct bands which are only observed for the ClEC-containing formulation. Around 470 cm<sup>-1</sup>, a band arises with increasing voltage, reaching its maximum at the cut-off voltage of 4.50 V. This band can be ascribed to semi-carbonates. [28] However, it can also be attributed to C-Cl stretching vibrations, [40] indicating that this band corresponds to a chlorinated decomposition product of ClEC, most likely a chlorinated organic carbonate, which also has been identified by the GC-MS measurements (See Supporting Information). Another distinct band is observed ≈1030 cm<sup>-1</sup>, present already for low potentials and showing increasing intensity with higher potentials. This band can be assigned to C-O stretching of semicarbonates as well, which corresponds to the decomposition of the electrolyte solvents or the additive. [28] Besides this band, two additional bands ≈1003 and 1080 cm<sup>-1</sup> are only identified for the ClEC-containing electrolyte. These bands can correspond to C—O stretching vibrations of either organic semi-carbonates<sup>[28]</sup> or Li<sub>2</sub>CO<sub>3</sub>.<sup>[26]</sup> Alternatively, these bands can be ascribed to poly-VC as well, indicating a similar polymerization reaction, as already known for FEC.[10,11,17] In contrast to the bands ≈470 and

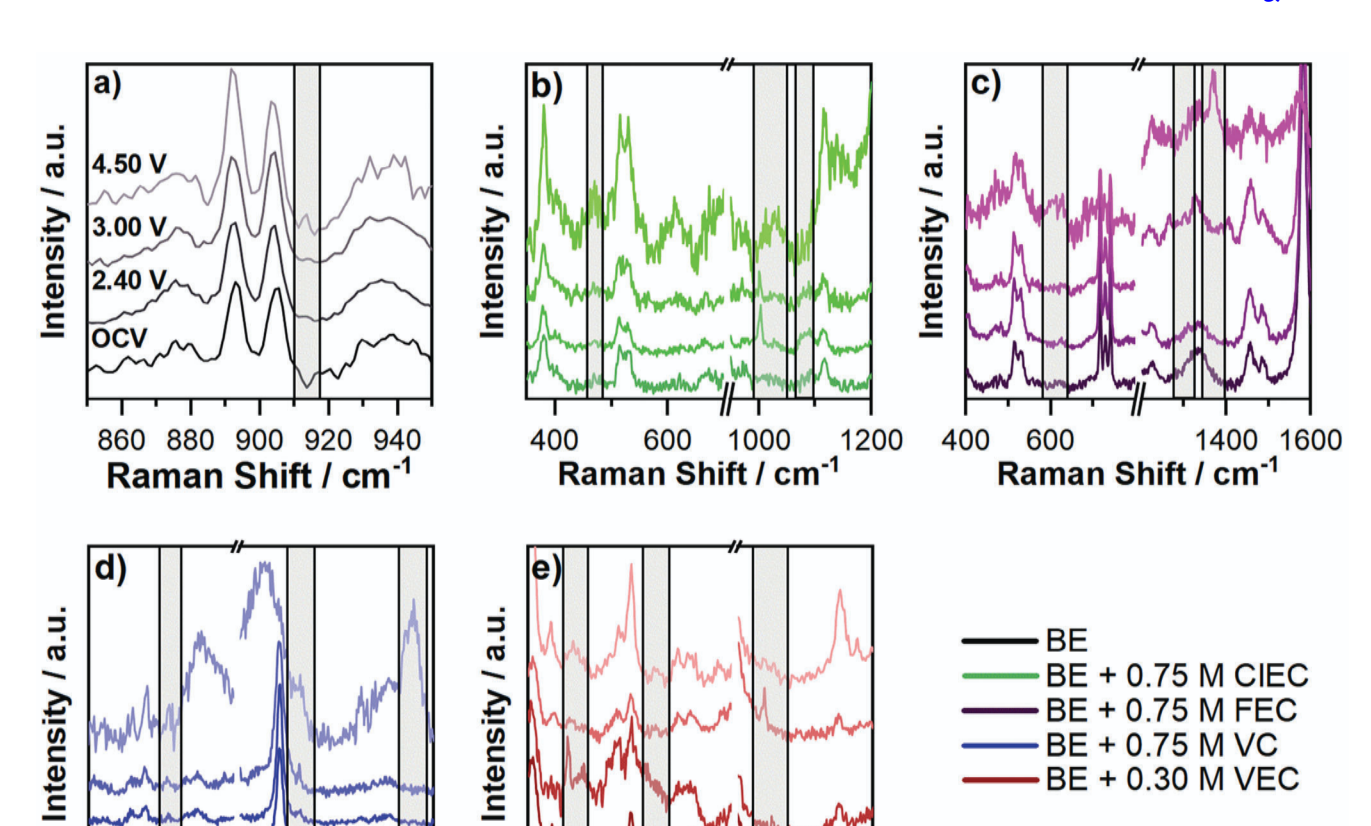


Figure 3. Results of the investigation of the surface layers formed on graphite anodes. a–e) Operando SHINER spectra taken of the surface of a graphite anode at different cell voltages in the presence of the following different electrolyte formulations: BE (baseline electrolyte, 1 μ LiPF<sub>6</sub> in EC:EMC 3:7, black), BE + 0.75 μ CIEC (green), BE + 0.75 μ FEC (purple), BE + 0.75 μ VC (blue), and BE 0.30 μ VEC (red). The spectra were taken at the OCV, 2.40, 3.00, and 4.50 V (bottom to top, decreasing color intensity equals higher cell voltages). Bands assigned to species characteristic for the investigated electrolyte formulation are highlighted by grey bars in the spectra. A detailed band analysis can be found in the Supporting Information.

1200

Raman Shift / cm<sup>-1</sup>

1800

1000

1030 cm<sup>-1</sup>, the intensity of the bands ≈1003 and 1080 cm<sup>-1</sup> decreases with increasing potential. This might indicate partial dissolution of the SEI, as already reported by Gajan et al.  $^{[28]}$ 

1800

For the FEC-containing electrolyte (Figure 3c), characteristic bands  $\approx$ 627, 1300, and 1370 cm<sup>-1</sup> are observed. While the band  $\approx$ 627 cm<sup>-1</sup> already rises at low potentials, the other bands are only identified for higher voltages, being especially distinct for the cut-off voltage of 4.5 V. All observed bands are in the known area of C–F deformation and stretching vibrations. [40] Nevertheless, the band  $\approx$ 627 cm<sup>-1</sup> could also correspond to LiOH, according to the literature, [41] while the other bands can alternatively be ascribed to C=O stretching vibrations of semi-carbonates, matching well with the expected decomposition products of FEC. [28] Additionally, the band  $\approx$ 1370 cm<sup>-1</sup> matches with a band from the reference spectrum of FEC, as well as C–C stretching bands of poly-thiophene and poly-furan. [42] Following these assignments, this band could indicate the presence of poly-FEC, which was already discussed by multiple studies. [10,11,17]

Surprisingly, the SHINER spectra of the electrode's surface in the presence of the VC-containing electrolyte, depicted in Figure 3d, do not exhibit any characteristic bands of polyVC.<sup>[26,43]</sup>

In general, the spectra of the VC-induced interphase show the least characteristic bands, except for the BE spectra. However, this is not surprising as VC does not possess any specific functional groups that could easily be distinguished from the carbonate-based electrolyte by Raman spectroscopy. Nevertheless, one characteristic band is identified  $\approx\!1160~\rm cm^{-1}$ , already arising at 2.40 V and exhibiting increasing intensity for higher voltages. This band can be attributed to semi-carbonates like lithium methyl carbonate (LMC), formed by the degradation of VC. [28] In addition to the discussed band, a distinct band  $\approx\!1854~\rm cm^{-1}$  was observed at the cut-off voltage of 4.50 V. This band can be attributed to the presence of Li<sub>2</sub>C<sub>2</sub>. [26]

For the VEC-containing electrolyte (Figure 3e), the SHINER spectra of the electrode's surface exhibit several characteristic bands  $\approx 1009$ , 1162, and 1639 cm<sup>-1</sup>. The band  $\approx 1009$  cm<sup>-1</sup> can only be identified for higher voltages, starting at 3.00 V. This band, as well as the band  $\approx 1162$  cm<sup>-1</sup>, can be assigned to semi-carbonate-like structures, for example, lithium ethyl methyl carbonate (LEMC), which could be formed by additive degradation. [28] The sharp band  $\approx 1639$  cm<sup>-1</sup> arises at 3.00 V and diminishes for higher voltages. Due to its proximity to

1000

1200

1600

Raman Shift / cm<sup>-1</sup>

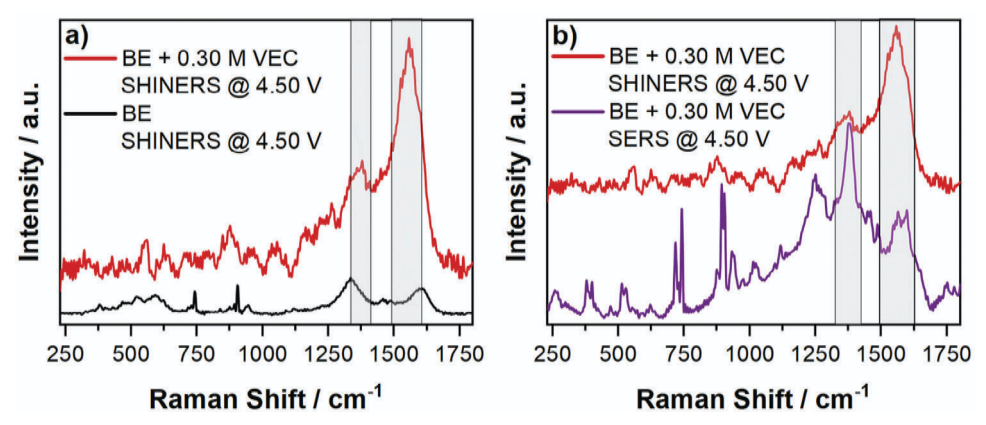


Figure 4. Results of the advanced near-field Raman spectroscopy investigation of the cathode surface in the presence of the BE (baseline electrolyte, 1  $\,\mathrm{M}$  LiPF $_6$  in EC:EMC 3:7) and the BE + 0.30  $\,\mathrm{M}$  VEC. a) Comparison of the operando SHINER spectra taken at a cathode potential of 4.50 V versus Li|Li<sup>+</sup> of the surface of an NMC622 electrode in the presence of the BE (black) and the BE + 0.30  $\,\mathrm{M}$  VEC (red). The comparison outlines the formation of an interphase on the cathodes' surface in the presence of VEC, as no additional prominent bands are observed for the BE spectrum. Characteristic bands, which are discussed in the main text, are marked with grey boxes. A detailed band assignment can be found in the SI. b) Comparison of the SHINER spectrum of an NMC622 electrode (red) and a SER spectrum of a roughened Au-electrode (purple) charged to a cathode potential of 4.50 V versus Li|Li<sup>+</sup> in the presence of the BE + 0.30  $\,\mathrm{M}$  VEC. The matching characteristic bands are highlighted in the spectra by grey boxes.

the band  $\approx 1651~\text{cm}^{-1}$ , which corresponds to the vinyl group of VEC, and the fact that this band's intensity decreases at elevated voltages, the band  $\approx 1639~\text{cm}^{-1}$  could correspond to a ring-opening reaction of the VEC molecule. At 4.50 V, the band  $\approx 1639~\text{cm}^{-1}$  only exhibits a very low intensity, while the band  $\approx 1651~\text{cm}^{-1}$  does not show its initial intensities again. This could indicate dissolution of the previously formed ring-opened VEC decomposition product from the anode's surface.

Overall it has to be noted that the results of the SHIN-ERS investigation of the different additive-induced SEIs lack a sophisticated explanation for the observed performance differences during galvanostatic cycling. Even so characteristic bands were identified for each investigated electrolyte formulation, in general, the influence of the additives mostly results in the enhanced formation of similar semicarbonates on the anode surface for every investigated electrolyte formulation.

### 2.3.2. CEI Investigation

As concluded from the previous section, the SHINERS investigation of the SEI composition did not provide a sufficient explanation for the enhanced performance of the VEC-based cells. In fact, the GC-MS experiments even indicated the formation of an ineffective SEI in the presence of VEC. Additionally, as discussed for the galvanostatic cycling results, roll-over failure, caused by cathode failure due to the high cut-off voltage, limits the cycle life of the cells. To determine the degradation state of the cycled electrodes, graphite anodes, and NMC622 cathodes were taken from NMC622||graphite pouch cells, cycled in the presence of the BE after their end-of-life (50% SoH). In coin cells, the aged electrodes were paired with pristine counterparts and cycled again in the BE. The obtained specific discharge capacities are depicted in Figure S10 (Supporting Information). While the aged anode paired with a fresh cathode exhibits discharge capacities similar

to the ones obtained from the original cycling experiment, the aged cathode paired with a fresh anode shows almost no cycling capability. This further outlines that the reason for the cell failure and severe capacity fading originates from the degradation of the cathode material. A previous study from our group already showed that the formation of a stable CEI is an effective approach to mitigate the effects of cathode degradation at high voltage.<sup>[31]</sup> Therefore, we investigated the CEI formation and composition in the presence of VEC.

Similar to the SEI investigation, initial SEM investigations of the NMC622 cathodes, electrochemically aged in the presence of the different electrolyte formulations, were performed (Figure S13, Supporting Information). The SEM images show clearly that only in the presence of VEC, does the formation of a CEI occur. Based on these results, operando SHINERS investigation of the surface of the NMC622 cathode in the presence of the BE and the BE +  $0.30~{\rm M}$  VEC was performed to elucidate interphase formation and composition (**Figure 4**). For the sake of clarity, we will only focus on the relevant active Raman bands. The full range SHINER spectra and detailed band assignments can be found in Figures S19 and S21 and Tables S6 and S8 (Supporting Information).

For the BE, no notable differences are observed in the SHINER spectra taken at the open-circuit potential (OCP) and at 4.50 V versus Li|Li<sup>+</sup> (Figure S21, Supporting Information). The observed bands can be attributed to the active vibrations of the cathode's active materials and the electrolyte.<sup>[44]</sup> These findings indicate that no significant CEI formation is to be expected in the presence of the BE, as already reported in previous studies from our group.<sup>[31,32]</sup>

In contrast to the BE, significant changes in the spectra can be observed in the presence of the VEC electrolyte, indicating CEI formation on the cathode's surface (Figure 4a; Figure S19, Supporting Information).

At the OCP, the spectrum is dominated by bands corresponding to the NMC active material  $\approx$ 530 and 595 cm<sup>-1</sup>,<sup>[44]</sup> the electrolyte species  $\approx$ 714, 730, 741, 874, 894, 904, and 936 cm<sup>-1</sup>,<sup>[30,44]</sup>

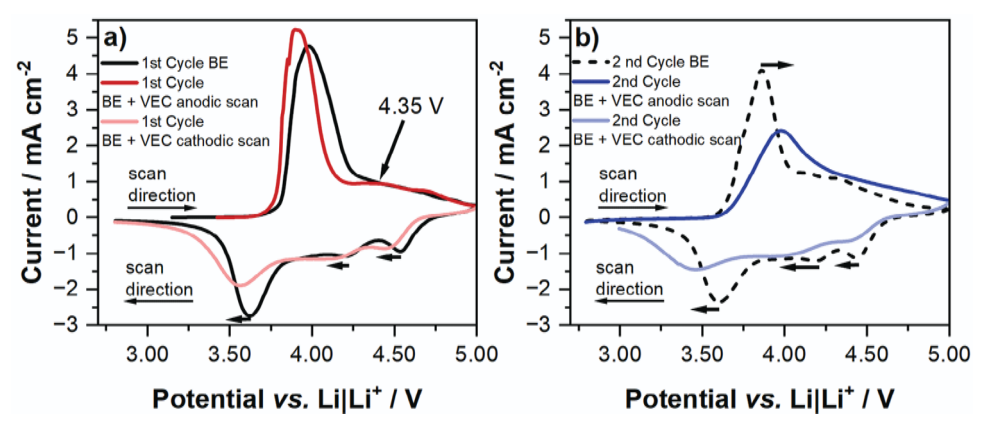


Figure 5. Cyclic voltammograms of the first (solid line) and second cycle (dashed line) of NMC622||graphite 3-electrode cells (lithium reference) of the BE (baseline electrolyte, 1 μ LiPF<sub>6</sub> in EC:EMC 3:7 black) in comparison to the BE + 0.50 μ VEC. For the VEC-containing electrolyte, the first cycle is marked in red, while the second cycle is marked in blue. To ease the identification anodic and cathodic parts of the VEC CV are marked with different color tones (anodic: dark, cathodic: light). The peak at 4.35 V, which is discussed in the main text is highlighted in a). In addition, peak shifts are also highlighted by arrows.

and the graphitic conducting agent  $\approx 1335$  and  $1600~\rm cm^{-1}$ . In addition, a band  $\approx 870~\rm cm^{-1}$  is observed which corresponds to VEC molecular vibration. With increasing electrode potentials new bands arise in the spectra starting at 3.30 V versus Li|Li<sup>+</sup> (Figure S19, Supporting Information). Most of these bands can be ascribed to different semi-carbonates, indicating the presence of VEC-derived species. [28,45] The bands  $\approx 1380$  and 1555 cm<sup>-1</sup> can be ascribed to the active vibration modes of alkyl-carbonates. [40,46] As shown in Figure 4a, these bands dominate the spectrum at 4.50 V, which indicates that alkyl-carbonate species form the majority of CEI composition in the cells containing VEC.

Even so, the conducted SHINERS investigation already shows the formation of a VEC-induced CEI, additional in situ SERS experiments were performed to confirm the results from the SHIN-ERS. SERS uses a gold substrate which prevents the overlap of the D- and G-bands of the graphitic conductive agent with the active Raman bands of the degradation products in the SHINER spectrum of the cathode surface. The SER spectra of the surface of the utilized Au-substrate in the presence of the BE as well as the VEC electrolyte are displayed in Figures \$20 and \$22 (Supporting Information) and a detailed band assignment can be found in Tables S7 and S9 (Supporting Information). In short, the in situ SERS results are in good agreement with the SHINERS investigation. No additional bands were observed in the SER spectra in the presence of the BE compared to the equivalent SHIN-ERS measurements, confirming that no significant CEI formation is to be expected in this electrolyte (Figure S22, Supporting Information). For the VEC electrolyte (Figure 4b; Figure S20, Supporting Information), the bands ≈1380 and 1550 cm<sup>-1</sup>, already identified in the operando SHINERS experiments are observed at 4.50 V versus Li|Li<sup>+</sup>. Additionally, a band  $\approx$ 1600 cm<sup>-1</sup>, which was covered in the SHINER spectra by the G-band of the conductive agent and also corresponds to carbonates, is identified as well. Moreover, a distinct band ≈267 cm<sup>-1</sup> can be observed only at 4.50 V. This band can be ascribed to the C-C deformation vibrations of aliphatic chains.[40] It has to be noted that the bands ascribed to carbonates only appear in the SER spectra at high potentials when compared to the SHINERS

measurements. However, this can be attributed to differences in the electrode materials, with Au as the WE for the SERS investigations.

### 2.3.3. Detailed CEI Analysis

The conducted advanced near-field Raman spectroscopy investigations of the cathode's surface outline the formation of a VEC-induced CEI. This is in good agreement with the physicochemical investigations and gives a plausible explanation for the contradicting results of the cycling experiments and the GC-MS measurements. Nevertheless, additional experiments were performed to further elucidate the origin of the VEC-derived interphase composition on the enhanced electrochemical performance of the respective cells.

To gain more insights into the oxidative behavior of the additives and their corresponding decomposition products, CV measurements of NMC622 cathode are performed (Figure 5). In the first anodic process in Figure 5a, the cyclic voltammogram of the VEC electrolyte exhibits an additional broad peak at 4.35 V versus Li|Li<sup>+</sup>, indicating a possible oxidation of the electrolyte additive. Already in the subsequent first cathodic process (Figure 5a) and second cycle anodic process (Figure 5b), the observed (de)intercalation peaks are notably broader and shifted, compared to the BE, indicating large cathode overpotentials in the presence of VEC. The CV investigation indicates CEI formation during the first charging process at high potentials, being in good agreement with the results of the Raman spectroscopy investigation. A detailed analysis of the CVs and the CVs of the other electrolyte formulations can be found in Figure S7 (Supporting Information).

On the graphite anode side, additional analyses were performed via FIB-SIMS with a time of flight (ToF) detector, with a focus on different Li-species (Li, LiF, and  $\rm Li_2O$ ), as well as Mn. The distribution of these species can indicate differences in the additive-induced interphases. While the presence of Li-species can be correlated to the reductive decomposition of electrolyte components and thus the SEI, Mn-species can be ascribed to

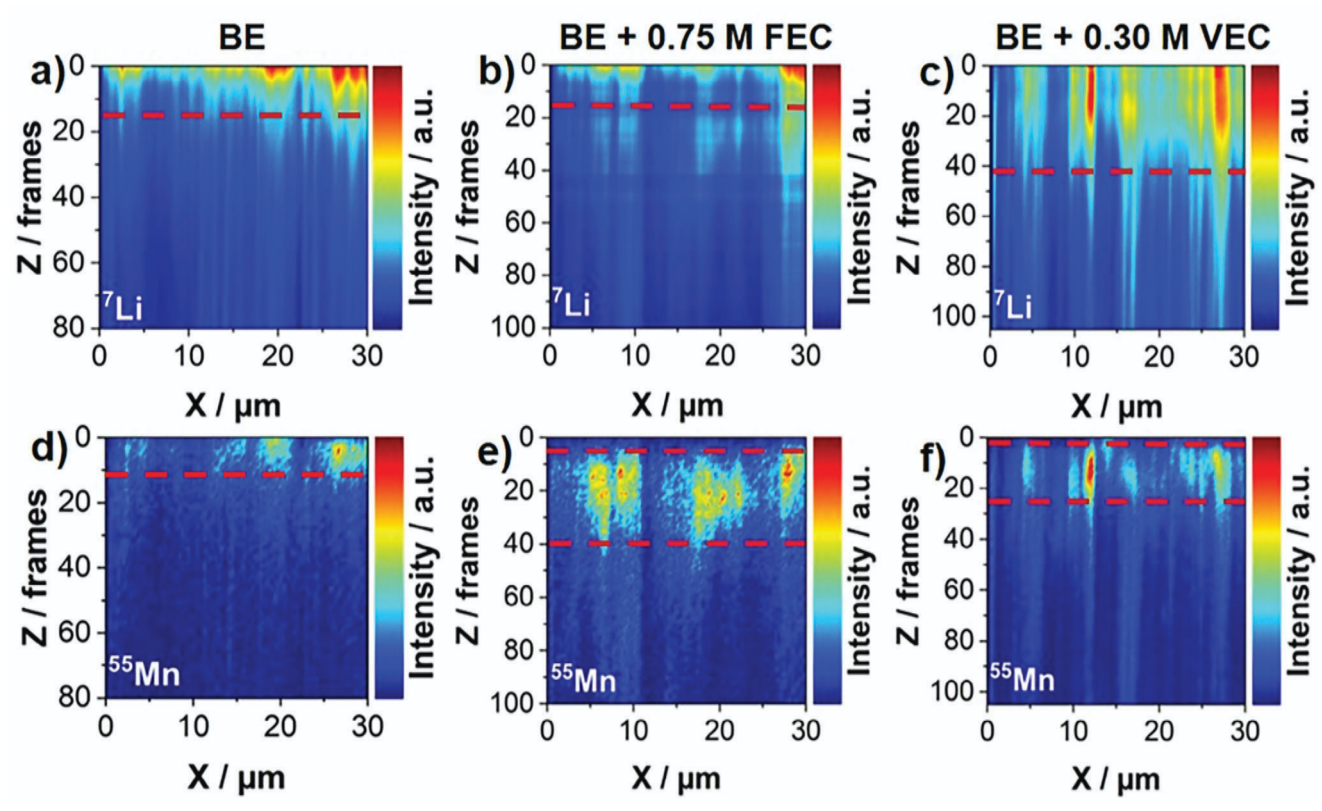


Figure 6. Results of the investigation of the surface layer on graphite electrodes taken from NMC622|graphite pouch-cells after reaching 50% state-of-health via focused ion beam secondary ion mass spectrometry (FIB-SIMS). Samples were taken from cells cycled with the BE (baseline electrolyte, 1 M LiPF<sub>6</sub> in EC:EMC 3:7, left column), BE + 0.75 M FEC (center column), and BE + 0.30 M VEC (right column). The images show the elemental spatial distribution of Li- (top row) and Mn- (bottom row) species. Areas of high element concentration are highlighted with dotted red lines.

the influence of the CEI on transition-metal dissolution and redeposition on the anode. As depicted in Figure 6, the obtained depth profiles of the graphite electrodes and the respective interphases show notable differences for the investigated electrolyte systems (additional FIB-SIMS images in Figures S32 and S33, Supporting Information). Comparing the depth profiles of the different Li-species, it can be observed that for the BE, FEC, and VC samples, the majority of Li-species is found in the very top layers of the electrodes. This indicates the formation of an effective SEI, preventing further electrolyte decomposition on the anode. In contrast, for CIEC and VEC, a deeper penetration depth of the Li-species into the electrode is observed. Especially, the findings for the VEC sample are in good agreement with the results of the GC-MS investigation, indicating the formation of an ineffective SEI, which leads to continuous electrolyte decomposition and the deposition of Li-species deeper in the electrode. A different trend can be observed for the Mn depth profile. While the majority of Mn is detected in the top layers for the BE, VC, and VEC samples, Mn is found also in deeper layers of the electrode for the FEC and ClEC samples. These findings indicate earlier Mn dissolution from the cathode active material for the FEC and CIEC samples, due to the formation of hydrofluoric acid (HF) and hydrochloric acid (HCl), etching transition metal from the cathode active material.[47,48] Again, these results are in good agreement with our suggestion of the formation of a VEC-induced CEI, suppressing transition-metal dissolution from the cathode active material and preventing roll-over failure.

## 2.4. Elucidating the VEC Cross-Talk Mechanism

As shown in Section 2.3 via in situ SERS and operando SHIN-ERS investigations, as well as additional CV and FIB-SIMS experiments, CEI formation occurs only in the presence of VEC. The results of the Raman spectroscopy investigations indicate that the CEI comprises semi-carbonates and alkyl-carbonates, with the latter making up the majority based on the relative intensity of the observed bands. Interestingly, the identified decomposition products are rather expected to be found on the anode than on the cathode due to the reductive mechanisms leading to their formation.<sup>[2,9]</sup> Finding them on the surface of the cathode would therefore either indicate an oxidative decomposition of the additive molecules or a cross-talk phenomenon, in which the additive molecules are reduced at the anode and transferred to the cathode. The former suggestion can be excluded, as no distinct oxidation peak was observed in the CV of the VEC electrolyte on the NMC622 WE at lower potentials (SHINERS investigations indicate CEI formation already ≈3.30 V versus Li|Li<sup>+</sup>).

To shed light on this phenomenon, the products of the reductive decomposition of VEC were synthesized, according to an

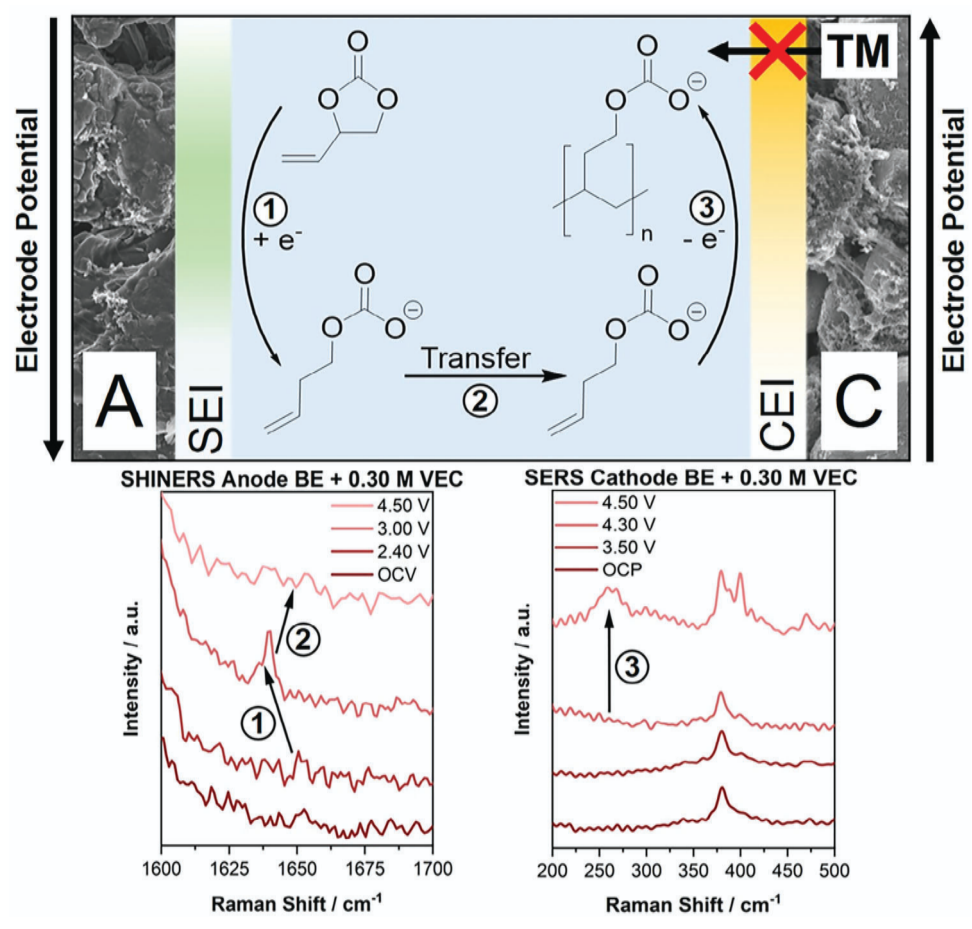


Figure 7. Schematic overview of the proposed VEC cross-talk phenomenon. Depicted is a schematic LIB consisting of a graphite anode (here as A) and an NMC622 cathode (here as C). Interphases formed on the electrode's surface are indicated by colored bars. Interphase formation and dissolution, in dependence on the electrode potential, are indicated by changes in the color's intensity. Important steps of the cross-talk mechanism are highlighted by numbers in the depicted reaction scheme: 1.: Reductive ring-opening of VEC, 2.: Dissolution and transfer of the VEC decomposition product from the anode to the cathode, 3.: electro-polymerization of the VEC decomposition product on the cathode surface, leading to the observed CEI formation, which is capable to suppress the dissolution of transition-metals (TM) to the electrolyte. The indicating numbers are picked up in advanced Raman spectra of the surface the respective electrodes in the presence of the BE (baseline electrolyte, 1 M LiPF<sub>6</sub> in EC:EMC 3:7) + 0.30 M VEC (left: Graphite anode (SHINERS), right: NMC622 cathode (SERS)) depicted below. The numbers are assigned to changes in the spectra which can be ascribed to the processes discussed in the schematic.

approach introduced by Lucht et al.[19,49] In this approach, naphthalene is treated with metallic Li to form lithium-naphthalenide, which is an acceptable model compound for studying the reactivity of the surface of the lithiated graphite anodes towards the investigated electrolyte formulation. This approach allows the formation of a significant amount of the decomposition products and enables their analysis with higher sensitivity using Raman spectroscopy. After the synthesis, the VEC decomposition products were suspended in THF and drop-cast on a SERS substrate. The SER spectrum of the decomposition product, in comparison with the in situ SER spectrum of the interphase on the Au-electrode in the presence of the VEC electrolyte, is depicted in Figure \$35 (Supporting Information). The comparison of the spectra shows clearly that especially the bands  $\approx$ 1380, 1550, and 1600 cm<sup>-1</sup>, attributed to the main components of the VECinduced CEI, are also present in the spectrum of the synthesized reduction product of VEC. This finding supports the approach that instead of oxidative decomposition, VEC molecules are actually chemically reduced on the anode side and subsequently transferred to the cathode, where they form an *effective* CEI. Further analysis of the synthesized VEC decomposition product was performed by cross-polarization magic-angle spinning (CP MAS)  $^{13}$ C $^{1}$ H $^{13}$ NMR, confirming carbonates, carboxylates, and alcoholates as products of the VEC reduction (Figures S36 and S37, Supporting Information).

To further elucidate the exact cross-talk mechanism and the resulting CEI composition, we performed a detailed analysis of the near-field Raman spectroscopy data in Section 2.3.1. According to **Figure 7**, 1) a notable shift of the band assigned to the characteristic VEC C=C double bond from 1651 to 1639 cm<sup>-1</sup> can be observed at a cell voltage of 3.00 V on the graphite anode (Figure 7, 1). Calculated Raman spectra indicate that this shift can be ascribed to a reductive ring-opening reaction of the VEC molecule on the anode surface (Table S10, Supporting Information), which is in good agreement with the performed CV measurements of VEC reduction (Figure S6, Supporting Information). Moreover,



www.advenergymat.de

additionally performed DFT calculations suggest the ring-opened VEC as a thermodynamically favored product of the VEC reduction (Figure \$39, Supporting Information). 2) At 4.50 V, the intensity of the band at  $1639~\mathrm{cm}^{-1}$ , now ascribed to ring-opened VEC, notably decreases on the anode. This finding implies the dissolution of the VEC ring-opened decomposition product from the anode's surface, allowing the transfer to the cathode side, most likely due to electro-migration. 3) In the SER spectra taken at high electrode potentials, no presence of a C=C double bond is observed. However, additional bands with low intensities ≈1027 and 1151, as well as a distinct band ≈267 cm<sup>-1</sup> arise in the SER spectra at 4.50 V versus Li|Li+. All of these bands can be ascribed to C−C stretching vibrations, with the band ≈267 cm<sup>-1</sup> being especially characteristic of C-C deformation vibrations of aliphatic chains.<sup>[40]</sup> As reported previously, molecules including vinylene groups can be oxidatively polymerized, [50] forming additional aliphatic C-C bonds. We therefore suggest that the ringopened VEC molecules polymerize on the cathode's surface at high electrode potentials, leading to the formation of an effective and non-soluble CEI. This conclusion is in good agreement with all previous results and gives a sophisticated explanation for the observed cycling performance of the VEC-containing cells. Nevertheless, we want to emphasize that the polymerization of the reductive degradation product of VEC only occurs at high potentials on the cathode. This strongly suggests that VEC only exhibits its beneficial CEI-forming behavior in high-voltage applications. In contrast, dedicated CEI-forming additives, like thiophenebased systems, show CEI-formation at notably lower cathode potentials, rendering their applicability also in nonhigh-voltage cells.[31]

# 3. Conclusion

In this study, different carbonate-based film-forming electrolyte additives were investigated in high-voltage NMC622||artificial graphite pouch-cells. It was observed that the addition of an optimized concentration of VEC to the electrolyte results in a significantly enhanced lifetime of the cells, and reduced capacity fading, notably outperforming common electrolyte additives like FEC or VC. Surprisingly, GC-MS experiments indicated that the VECinduced SEI is rather inefficient, exhibiting a transesterification that indicates reductive electrolyte decomposition. Additiveinduced CEI formation was finally shown by operando SHIN-ERS and in-situ SERS measurements of the cathode surface, supported by SEM and CV investigations. Semi-carbonates and especially alkyl-carbonates were identified as the main components of the VEC-based CEI. A comparison with the synthesized reduction product of VEC using lithium naphthalenide demonstrated that the VEC-degradation products identified in the formed CEI most likely originate from an initial chemical reduction of the additive by the lithiated graphite anode, followed by shuttling to the cathode. Detailed analysis of the obtained Raman spectra suggested an electro-polymerization of the VEC decomposition products on the cathode's surface after the cross-talk. The captured VEC-based CEI formation also explains the exceptional observed performance of the VEC cells, as the formed CEI most likely suppresses cathode active material degradation and prevents roll-over failure.

# 4. Experimental Section

Electrolyte Preparation: For the investigation and evaluation of the EC-based electrolyte additives, different electrolyte formulations were prepared. The additive-containing electrolyte formulations were prepared based on the baseline electrolyte (BE), consisting of 1.0 M lithium hexafluorophosphate (LiPF6, battery grade, E-Lyte Innovations, Germany) dissolved in EC and EMC (3:7 by weight, battery grade, E-Lyte Innovations, Germany), by the addition of FEC (98%, abcr GmbH, Germany), VC (battery grade, E-Lyte Innovations, Germany), CIEC (> 95%, Tokyo Chemical Industry Co., Japan) and VEC (99%, abcr GmbH, Germany) in different concentrations (0.05, 0.15, 0.50, and 0.75 M, additionally 0.30 M for VEC). Note that the volume of the utilized solvent mixture was adjusted to keep the concentration of LiPF6 in the resulting formulation at 1.0 M. All electrolyte formulations were prepared and stored in an argon-filled glovebox (MBraun, Germany, H2O, and O2 < 1 ppm).

Cell Preparation: Galvanostatic charge/discharge cycling of the electrolyte formulations was carried out using NMC622||artificial graphite commercial pouch-cells (Li-FUN Technology, Hunan, China) with an NMC622 active mass of 1.20 g and a nominal capacity of 200 mAh. Before cell assembly, the pouch cells were opened and dried under reduced pressure at 90 °C for 12 h. Afterward, the cells were filled with 700  $\mu L$  of electrolyte and massaged gently for  $\approx 5$  min to ensure sufficient wetting of the cell stack. The cells were vacuum-sealed on the upper end of the gas pocket at 165 °C for 5 s using a pouch-cell sealer (GN-HS350V, Gelon LIB Co., Shangdong, China). The sealing process was carried out at 15% of the ambient pressure. For degassing of the cells after formation, the cells were cut open and sealed directly at the cell stack under the aforementioned conditions. Preparation and degassing of the cells were carried out in a dryroom (dew point <-50 °C). Four cells were prepared for every considered electrolyte formulation to ensure reproducibility.

Potentiostatic characterization of the considered electrolyte formulations via CV was carried out using Swagelok T-type cells, allowing the use of a three-electrode configuration for precise determination of the electrode potential. For cell preparation, the inside of the Swagelok cells was covered with Mylar Foil (PET) to ensure electric insulation. WE and CE were separated by a 13 mm Whatman GF/D glass fiber separator, soaked with 120 µL of electrolyte. The RE was separated by an additional 10 mm Whatman GF/D glass fiber separator, soaked with 80 µL of electrolyte. The electrodes used for CV investigation were taken from the pouch cells. This was achieved by opening the cells, removing one side of the coating with THF (VWR, USA), and punching 12 mm diameter electrodes from the graphite and NMC622 electrode sheets. Before usage, the electrodes were dried at 90 °C under reduced pressure overnight. Cell preparation was performed in an argon-filled glovebox. For every investigated electrolyte formulation at least two cells were prepared to ensure reproducibility of the obtained cyclic voltammograms.

The 2032-type coin cells were prepared to evaluate the degradation of electrodes taken from pouch cells after reaching 50% SoH. Aged anodes and cathodes were paired with pristine counterparts. For coin cell assembly, 14 mm cathodes were paired with 15 mm anodes. The electrodes were separated by a 16 mm Celgard 2500 (polypropylene, Celgard, USA) separator, which was soaked with 60  $\mu L$  BE. Coin cell assembly was performed in a dry room.

Electrochemical Investigation: Galvanostatic charge/discharge cycling of the cells was carried out using a Maccor 4000 series battery tester in a voltage range from 4.50 to 2.80 V. Before cycling, the cells were prepolarized from open circuit voltage to 1.50 V for 12 h. For cell formation two charge/discharge cycles at C/10 with constant current/constant voltage (CCCV) steps were performed, followed by the degassing of the cells. Afterward, the cells were connected again to the battery tester and rested for 12 h before continuous constant current (CC) charge/discharge cycling at 1C. Galvanostatic charge/discharge cycling of the cells was performed in temperature-controlled chambers (BINDER, Germany) at 20 °C. To apply a constant pressure of ≈2 bar on the cell stack during charge/discharge cycling, the prepared cells were attached to specially designed cell holders. [51]



www.advenergymat.de

Potentiostatic investigations of the prepared electrolyte formulations were conducted via CV measurements, carried out on an Autolab Battery Tester (Metrohm, Switzerland) controlled by NOVA 2.1 (Metrohm, Switzerland) with a sweep rate of 150  $\mu$ V s $^{-1}$ . Cells with an NMC622||artificial graphite chemistry were tested between 2.80 and 5.00 V versus Li|Li $^+$ , and cells with a graphite||Li-metal cell chemistry were tested between 2.00 and 0.05 V. Li-metal was used as reference electrode for all CV measurements. CV experiments were performed for the BE and the BE with an additional 0.50 m of each investigated electrolyte additive. Before the measurement, the cells were rested for 10 h.

Nanoparticle Synthesis: For the SHINERS measurements, Aunanoparticles (NPs) with a 55 mm diameter and  $SiO_2$  coating were synthesized according to previous studies of our group. [31,32] In short, 100.00 mL of 0.01 wt.% AuCl<sub>3</sub> (>99.90%, Sigma-Aldrich, Germany) solution was added to a round bottom flask and brought to a boil. Afterward 0.70 mL of a 1 wt.% sodium citrate (reference standard, USP, USA) solution was added as quickly as possible under vigorous stirring. The solution was boiled for 30 min to obtain 55 mm Au-NPs. For the silica coating, 30.00 mL of the Au-NP solution was added to a round bottom flask. 0.40 mL of a 1.00 mm 3-aminopropyltrimethoxysilane (97%, Sigma Aldrich, Germany) solution was added dropwise under vigorous stirring. After 15 min of stirring at room temperature, 3.20 mL 0.54 wt.% sodium silicate (reagent grade, Sigma Aldrich, Germany) solution (pH 10, adjusted with HCl) was added. The resulting mixture was stirred for 3 min at room temperature. Afterward, the mixture was heated to 90 °C and stirred for 60 min. To stop further reactions, the mixture was subsequently cooled in an ice bath. The obtained mixture was centrifuged at 5000 rpm for 10 min at 10  $^{\circ}$ C. The supernatant was decanted and replaced with Milli-Q water. This washing step was repeated three times. The synthesized NPs were stored in a fridge at 6 °C.

All glassware utilized for the NP synthesis was cleaned with aqua regia beforehand. For the synthesis and the washing of the NPs, only MilliQwater (18.20 M $\Omega$  cm<sup>-1</sup>, Merck, Germany) was used.

Raman Sample Preparation: For this study, SERS and SHINERS measurements were performed, making two different sample preparations necessary. For the SHINERS measurements, the  $\mathrm{SiO}_2$ -coated NPs were drop-casted onto the investigated electrodes. To ease the casting process, the NPs were transferred from the aqueous medium to iso-propanol (>99.90%, Sigma Aldrich, Germany). Approximately 500  $\mu$ L of NP solution was cast on each respective electrode. After initial drying in a 110 °C oven, the electrodes were dried under reduced pressure at 90 °C overnight. The obtained electrodes were transferred and stored in an argon-filled glovebox.

For the SERS measurements, a gold foil (99.995%, ChemPUR, Germany) was first annealed using a gas burner until the electrode was glowing red. This state was held for at least 1 min. Afterward, the electrode was electrochemically roughened in a 0.10 m KCl (>99.50%, AppliChem, Germany) bath. Therefore, the gold electrode was cycled between -0.30 and +0.90 V versus Pt with a sweep rate of  $200\,\mu\text{V s}^{-1}$ . The potential was held at the ends of the sweep for 2 and 9 s, respectively. Platinum was used as CE and RE. Afterward, the electrode was cleaned with Milli-Q water and dried in an  $N_2$  stream.

For the operando Raman measurements, an airtight optical cell (ECC-Opto-Std, EL-CELL, Germany) was used. For SHINERS measurements, the investigated 10 mm electrode (graphite or NMC622, taken from pouch cells) was placed at the bottom of the cell with the active material facing the glass window. This electrode also serves as WE during the experiments. An additional Cu or Al mesh was placed on the WE to ensure sufficient electrolyte diffusion between the electrode and the glass window. The WE was covered with one layer of Celgard 2500 separator with a circular 4 mm cut-out in the middle. The CE (NMC622 for graphite WE, and  $\,$ graphite for NMC622 WE) with a circular cut-out in the middle was placed on top of the separator with its active material facing the WE. To determine the exact potential during the measurements on NMC622 electrodes, Limetal was used as RE. In an alternative electrode configuration, WE and CE were placed side-by-side, facing the optical window. For the SERS measurements, a similar set-up was used, featuring the roughened Au-electrode as WE at the bottom, topped by the separator and an NMC622 CE with circular cut-outs and a Li-metal RE. A detailed schematic of the optical cell and the electrode configuration can be found in Figure S1 (Supporting Information).

Finally, all cells were filled with  $\approx$ 200  $\mu$ L of electrolyte. Cell assembly was performed in an argon-filled glovebox.

Operando Raman Measurements: The Raman measurements were conducted using a confocal Raman microscope (LabRam Evolution HR, Horiba Scientific), equipped with an air-cooled CCD detector, a 600 line mm<sup>-1</sup> grating, and a 50X long-working distance objective (9.2 mm, numerical aperture 0.5, Zeiss, Germany). The samples were excited with a red laser (633 nm, 35 s, 3 x, 1.05 mW). Before every measurement, the system was calibrated to the peak of crystalline silicon at 520.70 cm<sup>-1</sup>. Operation of the Raman system, recording, and evaluation of the spectra were performed by using the LabSpec6.7.1.10 software (Horiba Scientific).

For the *operando* SHINERS measurements, galvanostatic charging of the optical cells was performed, while potentiostatic charging was performed for the SERS experiments, using an Autolab potentiostat/galvanostat PGSTAT204 (Metrohm, Switzerland) controlled by the NOVA 2.1 software (Metrohm, Switzerland). For the SHINERS measurements, the optical cells were charged to 4.50 V by applying a current calculated based on the capacity of the respective WE, resembling a C-rate of C/3. Raman measurements were performed at the OCV and cell voltage of 2.40, 3.00, and 4.50 V. During Raman measurements, a constant voltage was applied to the electrode to avoid a voltage drop. For the SERS measurements a linear sweep voltammetry (LSV) experiment was performed, charging the WE up to a potential of 4.50 V versus Li|Li+ with a sweep rate of 150 µV s<sup>-1</sup>. Raman measurements were performed at the OCP and potentials of 3.50, 3.80, 4.00, 4.20, and 4.50 V versus Li|Li+.

GC-MS Measurements: After 100 galvanostatic charge/discharge cycles, the electrolyte was extracted from the cells and investigated employing gas GC-MS. In detail, after galvanostatic charge/discharge cycling, the cells were transferred and opened in an argon-filled glovebox. Then, the cell stack was removed and the electrodes were separated. The anode and the separator were transferred to a centrifugation system introduced by Horsthemke et al.<sup>[52]</sup> The samples were centrifuged at 8000 rpm for 30 min and 20 °C using a MEGA STAR 600R centrifuge (VWR, USA). The obtained electrolyte was diluted 1:100 (ν:ν) in dichloromethane and rested overnight at 5 °C to precipitate the LiPF<sub>6</sub> conducting salt. GC-MS experiments were carried out on a Shimadzu GCMS-QP2010 Ultra equipped with an AOC-5000 Plus autosampler and a nonpolar Supelco SLB-5 ms (30 m  $\times$  0.25 mm. 0.25  $\mu$ m, Sigma Aldrich) column. For the measurements, a sample volume of 1 µL was injected and the GC injector was set to 250 °C. The initial oven temperature was set to 40 °C, held for 1 min, and subsequently increased by two ramps of 3 K min<sup>-1</sup> to 60 and 30 K min<sup>-1</sup> to 260  $^{\circ}$ C. The final temperature was held for 2 min. The ion source was operated in electron ionization mode with 70 eV and the detector voltage was set according to a weekly auto-tune. The quadrupole mass detector was operated in scan mode in an m/z range from 20 to 350.

FIB-SIMS Analysis: The chemical analysis of the SEI was further assessed with a FIB-SIMS technique, using the fibTOF detector from TOFW-ERK. fibTOF is a time-of-flight (TOF) mass analyzer mounted on a FIB-equipped SEM microscope. [53] The ion gun supplies the fibTOF with primary ions (in this case  $^{69}\text{Ga}^+$ ). The ions are focused on the sample where they cause a collision cascade, resulting in the emission of charged and neutral particles from the surface. The released secondary ions were collected for analysis by the fibTOF ion extractor and electrostatically pulsed in an orthogonal direction to the detector. After the initial acceleration, the ions drift along a field-free distance called the flight tube, where they are dispersed in time according to their different velocities, which depend on their mass-to-charge ratio (m/q), e.g., the lower the mass of the ion, the faster it was. The chemical nature of the ejected ions was thus determined by measuring the flight time required to drift along the tube. [54]

Synchronization of the SIMS signal with the FIB scan pattern produces a 3D data set as the FIB beam repeatedly scans the sample surface. The dwell time per voxel is typically set to  $\geq\!10~\mu s$ , allowing a mass range of 1–500 Th to be recorded. This type of analyzer measures a complete mass spectrum (e.g., all present elements and their corresponding isotopes)

www.advenergymat.de

Received: May 21, 2024

Published online: July 18, 2024

Revised: July 8, 2024

for each probed voxel. The highly focusable beam and the relatively low penetration depth of the primary ions (compared to electrons) allow the investigation of local composition with nanometer resolution.[55] SIMS allows the analysis of all elements in the periodic table and is particularly sensitive to alkali metals, alkaline earth metals, and halogens, which have high secondary ion yields. These characteristics make FIB-SIMS an ideal technique for studying the SEI of Li-ion batteries.

Six different graphite anodes were studied, one pristine, four cycled to the end of their life (50% SoH) in the presence of the investigated additives, and one control sample cycled with the BE. The cells were opened in an argon-filled glovebox to extract the electrode samples. The samples were dried under a reduced atmosphere in the glovebox antechamber for 10 min to remove electrolyte solvent residues and stored in an argon atmosphere. The FIB current was set to 30 keV and 1 nA, and the field of view was adjusted to 30 μm.

It has to be mentioned that due to the similarity of the sample's composition, it can be assumed that the ablated layers (1 frame = 1 layer) have an equal thickness allowing the direct comparison of the obtained depth profiles.

Synthesis of Reductive Decomposition Products: To reveal the origin of the VEC decomposition products, identified on the cathode surface, the reduction product of VEC was synthesized according to Lucht et al.[19,49] In a 100 mL round-bottom flask 4.09 g (0.032 mol) naphthalene (98%, TCI, Japan) was dissolved in 50 mL dry THF (solvent purification system, Pure-Solv MD 7 Euro, inertcorp, USA). Subsequently, 0.20 g (0.029 mol) lithiummetal (Albemarle, USA) was added to the flask. Immediately, the solution turned into a dark green. The obtained mixture was stirred overnight at room temperature. VEC (99%, abcr GmbH, Germany) was added in a 1:1 molar ratio (3.31 g) to the flask. Upon the addition of VEC, the reaction mixture turned to a red-yellowish color. The reaction mixture was stirred overnight at room temperature. Afterward, the solvent was removed by high vacuum, and the obtained precipitate was washed five times with 20 mL dry diethyl ether (solvent purification system, PureSolv MD 7 Euro, inertcorp, USA). The final product was obtained as a yellow powder and dried under a high vacuum before further analysis via SERS using an AgAu SERS substrate (SERSitive, Poland) and cross-polarization magic-angle spinning NMR. The product was soluble in water but remained insoluble in organic solvents.

# **Supporting Information**

Supporting Information is available from the Wiley Online Library or from the author.

# Acknowledgements

Financial support from the German Federal Ministry for Education and Research within the project EFoBatt (grant number 13XP5129) is gratefully acknowledged. The authors gratefully thank Johannes Thienenkamp, Sascha Peters, and Dr. Gunther Brunklaus for performing the CP MAS NMR measurement.

Open access funding enabled and organized by Projekt DEAL.

# Conflict of Interest

The authors declare no conflict of interest.

# **Data Availability Statement**

The data that support the findings of this study are available from the corresponding author upon reasonable request.

# Keywords

cross-talk, electrolyte additive, interphase, lithium-ion batteries, operando **SHINERS** 

- [1] H. Adenusi, G. A. Chass, S. Passerini, K. V. Tian, G. Chen, Adv. Energy Mater. 2023, 13, 2203307.
- [2] S. J. An, J. Li, C. Daniel, D. Mohanty, S. Nagpure, D. L. Wood, Carbon **2016** 105 52
- [3] M. Weiling, F. Pfeiffer, M. Baghernejad, Adv. Energy Mater. 2022, 12, 2202504
- [4] J.-F. Ding, R. Xu, C. Yan, B.-Q. Li, H. Yuan, J.-Q. Huang, J. Energy Chem. **2021**, *59*, 306.
- [5] H. Zhao, X. Yu, J. Li, B. Li, H. Shao, L. Li, Y. Deng, J. Mater. Chem. A **2019**, 7, 8700.
- [6] S. Klein, K. Borzutzki, P. Schneider, O. Fromm, J. Reiter, Q. Fan, T. Placke, M. Winter, J. Kasnatscheew, Chem. Mater. 2020, 32, 6279.
- [7] L. Quach, E. Adhitama, V. Göldner, A. Das, F. Demelash, M. Winter, U. Karst, T. Placke, F. Glorius, ACS Appl. Energy Mater. 2023, 6, 9837.
- [8] M. Winter, Zeitschr. Physika. Chem. 2009, 223, 1395.
- [9] S. S. Zhang, J. Power Sources 2006, 162, 1379.
- [10] M. Nie, J. Demeaux, B. T. Young, D. R. Heskett, Y. Chen, A. Bose, J. C. Woicik, B. L. Lucht, J. Electrochem. Soc. 2015, 162, A7008.
- [11] B. N. Olana, L. H. Adem, S. D. Lin, B.-J. Hwang, Y.-C. Hsieh, G. Brunklaus, M. Winter, ACS Appl. Energy Mater. 2023, 6, 4800.
- [12] P. Yan, M. Shevchuk, C. Wölke, F. Pfeiffer, D. Berghus, M. Baghernejad, G.-V. Röschenthaler, M. Winter, Small Struct. 2024, 5, 2300425.
- [13] B. A. Sadeghi, C. Wölke, F. Pfeiffer, M. Baghernejad, M. Winter, J. Power Sources 2023, 557, 232570.
- [14] A. Ghaur, F. Pfeiffer, D. Diddens, C. Peschel, I. Dienwiebel, L. Du, L. Profanter, M. Weiling, M. Winter, T. Placke, S. Nowak, M. Baghernejad, Small 2023, 19, e2302486.
- [15] S.-K. Jeong, M. Inaba, R. Mogi, Y. Iriyama, T. Abe, Z. Ogumi, Langmuir **2001**, *17*, 8281.
- [16] J. Chai, Z. Liu, J. Ma, J. Wang, X. Liu, H. Liu, J. Zhang, G. Cui, L. Chen, Adv. Sci. 2017, 4, 1600377.
- [17] Y. Kamikawa, K. Amezawa, K. Terada, J. Phys. Chem. C 2020, 124, 19937.
- [18] H. Ota, Y. Sakata, Y. Otake, K. Shima, M. Ue, J. Yamaki, J. Electrochem. Soc. 2004, 151, A1778.
- [19] A. L. Michan, B. S. Parimalam, M. Leskes, R. N. Kerber, T. Yoon, C. P. Grey, B. L. Lucht, Chem. Mater. 2016, 28, 8149.
- [20] V. Etacheri, O. Haik, Y. Goffer, G. A. Roberts, I. C. Stefan, R. Fasching, D. Aurbach, Langmuir 2012, 28, 965.
- [21] Q. Zhang, S. Liu, Z. Lin, K. Wang, M. Chen, K. Xu, W. Li, Nano Energy 2020, 74, 104860.
- [22] F. Meng, S. Zhu, J. Gao, F. Zhang, D. Li, Ionics 2021, 27, 3821.
- [23] S. Y. Lee, Y. J. Park, ACS Omega 2020, 5, 3579.
- [24] Z. X. Shu, R. S. McMillan, J. J. Murray, I. J. Davidson, J. Electrochem. Soc. 1995, 142, L161.
- [25] J. Maibach, J. Rizell, A. Matic, N. Mozhzhukhina, ACS Mater. Lett. **2023**, 5, 2431.
- [26] S. Hy, Felix, Y.-H. Chen, J. Liu, J. Rick, B.-J Hwang, J. Power Sources 2014, 256, 324,
- [27] V. Stancovski, S. Badilescu, J. Appl. Electrochem. 2014, 44, 23.
- [28] A. Gajan, C. Lecourt, B. E. Torres Bautista, L. Fillaud, J. Demeaux, I. T. Lucas, ACS Energy Lett. 2021, 6, 1757.
- [29] N. Gogoi, T. Melin, E. J. Berg, Adv. Mater. Inter. 2022, 9, 2200945.
- [30] N. Mozhzhukhina, E. Flores, R. Lundström, V. Nyström, P. G. Kitz, K. Edström, E. J. Berg, J. Phys. Chem. Lett. 2020, 11, 4119.
- [31] F. Pfeiffer, D. Diddens, M. Weiling, L. Frankenstein, S. Kühn, I. Cekic-Laskovic, M. Baghernejad, Adv. Energy Mater. 2023, 13, 2300827.

16146840, 2024, 39, Downloaded from https://advanced.onlinelibrary.wiley.com/doi/10.1002/acmm.202402187 by Universitäts- und Landesbibliothek Münster, Wiley Online Library on [15/10/2025]. See the Terms

(https://onlinelibrary.wiley.com/terms

-and-conditions) on Wiley Online Library for rules of use; OA articles are governed by the applicable Creative Commons License



- [32] F. Pfeiffer, D. Diddens, M. Weiling, M. Baghernejad, ACS Appl. Mater. Interfaces 2023, 15, 6676.
- [33] L. Cabo-Fernandez, D. Bresser, F. Braga, S. Passerini, L. J Hardwick, Batteries Supercaps 2019, 2, 168.
- [34] D. Martín-Yerga, D. C. Milan, X. Xu, J. Fernández-Vidal, L. Whalley, A. J. Cowan, L. J. Hardwick, P. R. Unwin, Angew. Chem. Int. Ed. Engl. 2022, 61, e202207184.
- [35] S. Klein, S. van Wickeren, S. Röser, P. Bärmann, K. Borzutzki, B. Heidrich, M. Börner, M. Winter, T. Placke, J. Kasnatscheew, Adv. Energy Mater. 2021, 11, 2003738.
- [36] S. Klein, P. Bärmann, T. Beuse, K. Borzutzki, J. E. Frerichs, J. Kasnatscheew, M. Winter, T. Placke, ChemSusChem 2021, 14, 595.
- [37] I. Buchberger, S. Seidlmayer, A. Pokharel, M. Piana, J. Hattendorff, P. Kudejova, R. Gilles, H. A. Gasteiger, J. Electrochem. Soc. 2015, 162, A2737.
- [38] L. Haneke, J. E. Frerichs, A. Heckmann, M. M. Lerner, T. Akbay, T. Ishihara, M. R. Hansen, M. Winter, T. Placke, J. Electrochem. Soc. **2020**, 167, 140526.
- [39] M. Weiling, C. Lechtenfeld, F. Pfeiffer, L. Frankenstein, D. Diddens, J.-F. Wang, S. Nowak, M. Baghernejad, Adv. Energy Mater. 2023, 14, 2303568.
- [40] G. Socrates, Infrared and Raman Characteristic Group Frequencies: Tables and Charts, 3rd ed., Wiley, Chichester 2010.
- [41] S. Tang, Y. Gu, J. Yi, Z. Zeng, S.-Y. Ding, J.-W. Yan, D.-Y. Wu, B. Ren, Z.-Q. Tian, B.-W. Mao, J. Raman Spectr. 2016, 47, 1017.
- [42] F. Alakhras, R. Holze, Electrochim. Acta. 2007, 52, 5896.
- [43] H. Ota, Y. Sakata, A. Inoue, S. Yamaguchi, J. Electrochem. Soc. 2004, 151, A1659.

- [44] C.-Y. Li, Y. Yu, C. Wang, Y. Zhang, S.-Y. Zheng, J.-F. Li, F. Maglia, R. Jung, Z.-Q. Tian, Y. Shao-Horn, J. Phys. Chem. C. 2020, 124, 4024.
- [45] G. Li, H. Li, Y. Mo, L. Chen, X. Huang, J. Power Sources 2002, 104, 190.
- [46] T. Schedlbauer, S. Krüger, R. Schmitz, R. W. Schmitz, C. Schreiner, H. J. Gores, S. Passerini, M. Winter, Electrochim. Acta. 2013, 92, 102.
- [47] H. Zhang, Z. Zeng, F. Ma, X. Wang, Y. Wu, M. Liu, R. He, S. Cheng, J. Xie, Adv. Funct. Mater. 2023, 33, 2212000.
- [48] M. Hekmatfar, I. Hasa, R. Eghbal, D. V. Carvalho, A. Moretti, S. Passerini, Adv. Mater. Inter. 2020, 7, 1901500.
- [49] M. Nie, D. Chalasani, D. P. Abraham, Y. Chen, A. Bose, B. L. Lucht, J. Phys. Chem. C. 2013, 117, 1257.
- [50] H. J. Santner, K.-C. Möller, J. Ivančo, M. G. Ramsey, F. P. Netzer, S. Yamaguchi, J. O. Besenhard, M. Winter, J. Power Sources 2003, 119-121, 368.
- [51] J.-P. Schmiegel, M. Leißing, F. Weddeling, F. Horsthemke, J. Reiter, Q. Fan, S. Nowak, M. Winter, T. Placke, J. Electrochem. Soc. 2020, 167,
- [52] F. Horsthemke, V. Winkler, M. Diehl, M. Winter, S. Nowak, Energy Tech. 2020, 8, 1801081.
- [53] L. Pillatsch, F. Östlund, J. Michler, Prog. Cryst. Growth Charact. Mater. 2019, 65, 1,
- [54] E. de Hoffmann, V. Stroobant Mass Spectrometry: Principles and Applications, 3rd ed., Wiley, Chichester, Weinheim 2007.
- [55] J. A. Whitby, F. Östlund, P. Horvath, M. Gabureac, J. L. Riesterer, I. Utke, M. Hohl, L. Sedláček, J. Jiruše, V. Friedli, M. Bechelany, J. Michler, Adv. Mater. Sci. Eng. 2012, 2012, 1.